NANO LETTERS

Letter

pubs.acs.org/NanoLett

Surfactant Organic Molecules Restore Magnetism in Metal-Oxide Nanoparticle Surfaces

Juan Salafranca,*[,†,‡,#] Jaume Gazquez,[†,‡,#,▽] Nicolás Pérez,[§] Amílcar Labarta,[§] Sokrates T. Pantelides,[∥,‡] Stephen J. Pennycook,[‡,∥] Xavier Batlle,[§] and Maria Varela[‡,†]

[†]Dpt. Física Aplicada III, Universidad Complutense de Madrid, Madrid, 28040 Spain

[‡]Materials Science and Technology Division, Oak Ridge National Laboratory, Oak Ridge, Tennessee 32831, United States

[§]Dpt. Fisica Fonamental and Institut de Nanociència i Nanotecnologia (IN2UB), Universitat de Barcelona, 08028 Barcelona, Spain

[∥]Department of Physics and Astronomy, Vanderbilt University, Nashville, Tennessee 37235, United States

Supporting Information

ABSTRACT: The properties of magnetic nanoparticles tend to be depressed by the unavoidable presence of a magnetically inactive surface layer. However, outstanding magnetic properties with a room-temperature magnetization near the bulk value can be produced by high-temperature synthesis methods involving capping with organic acid. The capping molecules are not magnetic, so the origin of the enhanced magnetization remains elusive. In this work, we present a real-space characterization on the subnanometer scale of the magnetic, chemical, and structural properties of iron-oxide nanoparticles via aberration-corrected scanning transmission electron microscopy. For the first time, electron magnetic chiral dichroism is used to map the magnetization of nanoparticles in real space with subnanometer spatial resolution. We find that the surface of the nanoparticles is magnetically ordered. Combining the results with density functional calculations, we establish how magnetization is restored in the surface layer. The bonding with the acid's O atoms results in O−Fe atomic configuration and distances close to bulk values. We conclude that the nature and number of molecules in the capping layer is an essential ingredient in the fabrication of nanoparticles with optimal magnetic properties.

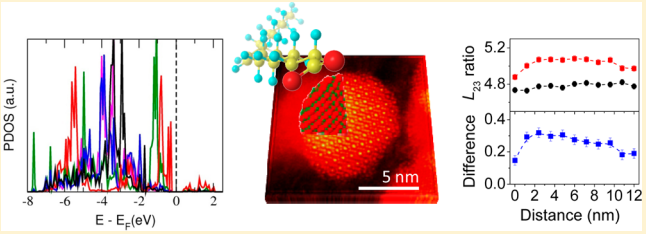

KEYWORDS: *Ferrites, metal-oxide nanoparticles, magnetism, electron magnetic chiral dichroism, electron energy loss spectroscopy*

Metal-oxide nanoparticles show complex magnetic behaviors including a significant reduction of the magnetization at the surface layer, which makes them unfit for applications such as magnetic-field-assisted drag and removal of cancer cells, magnetically directed drug delivery, magnetic heating or elimination of tumors.[1−8] However, magnetite (Fe_3O_4) nanoparticles prepared by high-temperature decomposition of iron precursors in an organic medium with different organic acids[2−4] exhibit an unusually high magnetization, near the bulk value at room temperature. These properties may be related to the fact that such high-temperature synthesis conditions promote high crystallinity.[9−11] It has also been suggested that the iron−carboxylic group bonding plays a determining role during synthesis.[12−14] The resulting bond between the organic acid and the nanoparticles would prevent further oxidation to Fe_2O_3, which could be detrimental for magnetization.[15] Recently, in a related system, it has been observed that atomic H bonds to surface O atoms in magnetite thin films and affects the spin polarization at the Fermi energy,[16,17] but the mechanism underlying the unexpectedly high magnetization of Fe_3O_4 nanoparticles remains far from understood.

In this Letter, we study the unusual magnetic properties of high-quality Fe_3O_4 nanoparticles by means of advanced electron microscopy techniques combined with theoretical calculations. For the first time, we use electron magnetic chiral dichroism in the aberration-corrected electron microscope to produce real-space maps of magnetization with subnanometer resolution. Our results show that not only the nanoparticle volume but also the surface presents bulk-like magnetization at room temperature. Combining these results with density functional calculations, we establish the key role of the nonmagnetic organic acid capping layer. The bonding with the acid's O atoms results in surface O−Fe atomic configurations and distances close to bulk values. By promoting a bulk-like environment, the nonmagnetic ligands restore magnetism in the surface layer. Our results highlight the importance of the optimization of nanoparticle properties by improving synthesis processes and more flexible functionalizing routes,[9,18,19] which will pave the way to the next generation of applications.[5−8]

Our magnetite nanoparticles, synthesized at high temperatures with oleic acid as a surfactant, show a room-temperature saturation magnetization ∼80% of that of the bulk.[1,11] To

Received: February 16, 2012
Revised: April 4, 2012
Published: April 12, 2012

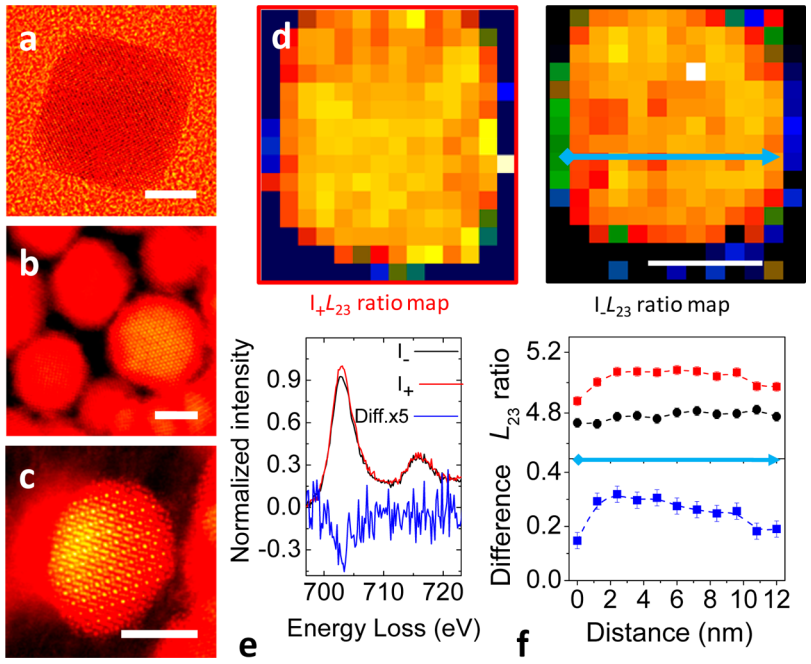

Figure 1. Real-space magnetization characterization with nanometer resolution. (a) Aberration-corrected STEM bright-field image of a Fe_3O_4 nanoparticle. (b,c) High-resolution Z-contrast STEM images of two Fe_3O_4 nanoparticles along the ⟨111⟩ and the ⟨01̄1⟩ zone axes, respectively, showing high crystal quality. Nominal particle sizes are 9 and 5 nm, respectively. The spherical shape of these very small particles is due to the greater relative importance of the surface formation energy. (d) Color-coded $L_{2,3}$ ratio maps obtained from the spectrum image of the nanoparticle shown in panel a acquired at symmetric positions in the diffraction pattern: I_+ (left) and at I_-, (right), respectively. (e) Averaged EELS spectra in the Fe $L_{2,3}$ edges, after background subtraction, for the nanoparticle shown in panel a measured at I_+ and I_- and the resultant dichroic signal (in blue), represented by the difference, which has been magnified by a factor of 5 in the Figure. The spectra were normalized to the background region between the two edges. (f) Top: $L_{2,3}$ profile along the direction of the blue arrow in panel d (in red and in black for I_+ and I_- L_{23} ratio maps, respectively). Bottom: difference between I_+ and I_- $L_{2,3}$ ratios along the nanoparticle. The scale bar represents 5 nm in all panels. Images in false color.

clarify the origin of this unusually high magnetization, we studied nanoparticles with sizes from 6 to 15 nm. Real-space characterization of crystal structure, magnetism, and spectroscopy was performed by aberration-corrected scanning transmission electron microscopy (STEM). The Supporting Information contains more details of the setup and the procedure that leads to the spectra-derived maps. Figure 1a shows a STEM bright field image of a nanoparticle 13 nm in size, exhibiting an extremely high crystal quality. Even for the smallest particle sizes they are monodomain, and the crystal structure is maintained all the way to the surface. (See Figure 1b,c).

Electron energy loss spectroscopy (EELS) in the electron microscope can be used to probe the local magnetization at room temperature. Similarly to X-ray magnetic circular dichroism (XMCD), electron magnetic chiral dichroism (EMCD) utilizes the $L_{2,3}$ EELS absorption edges of transition metals obtained from either wide specimen areas[20] or regions of a few nanometers in size.[21,22] Here we show for the first time how an EMCD signal can also be obtained with an electron beam ∼1 nm in diameter, operating in nanodiffraction mode. (See the Supporting Information.)

The difference in the room-temperature iron $L_{2,3}$ edges (Figure 1e) coming from conjugated spots in the nanodiffraction diagram (equivalent to the two beam polarizations used in XMCD measurements[20]) is proportional to the local magnetic moment. Figure 1d shows two $L_{2,3}$ ratio maps obtained from a spectrum image of the nanoparticle in Figure 1a. The difference in $L_{2,3}$ ratio profiles in Figure 1f indicates that the magnetic moment within 1 nm of the particle surface is at most 30% smaller than the magnetization of the core, even at room temperature. To our knowledge, no real-space nanoscale resolution magnetization density map has been previously reported. This finding is in sharp contrast with results from nanoparticles prepared through other methods,[1] which show a disordered spin structure at the particle surface. In our case, the highly magnetic surface is strongly contributing to the high saturation magnetization of these high crystal quality nanoparticles near room temperature.[15] The question to be addressed then is how this unexpectedly high surface magnetization is stabilized.

Aberration-corrected STEM-EELS provides further unique insight into this issue. Figure 2a shows significant variations of O and Fe concentration. The centers of the nanoparticles show an O atomic ratio of 57%, which is consistent with a Fe_3O_4 magnetite structure. (See Figure 2b.) However, a clear increase in the oxygen atomic ratio at the surface is observed. The extra oxygen comes from the carboxylic group of the oleic acid used in the synthesis, which is attached to the surface. This picture is confirmed by EELS fine-structure analysis and theoretical calculations. In bulk iron oxides, it has been demonstrated that the intensity of the prepeak in the O *K* edge (normalized to the main peak) and the intensity ratio of the Fe L_2 and L_3 white lines increases with the iron oxidation state.[23] However, despite a richer oxygen content, both the prepeak intensity and the L_{23} ratio (Figure 3a,b) clearly decrease at the surface. Both observations indicate a more reduced Fe,[23] which is the opposite of what would be expected from the observed higher O concentration.

dx.doi.org/10.1021/nl300665z | *Nano Lett.* 2012, 12, 2499−2503

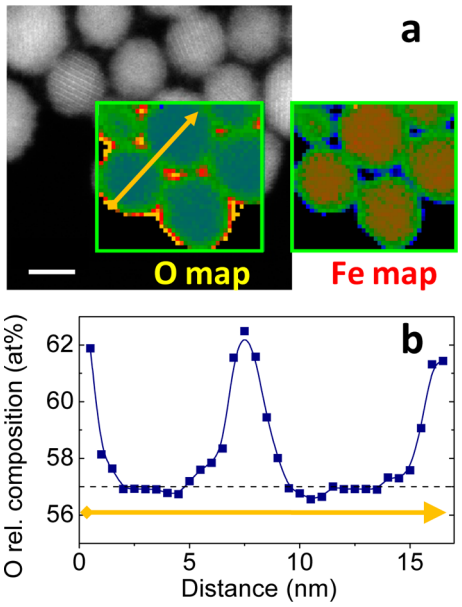

Figure 2. Chemical composition maps. (a) Low-magnification Z-contrast image. The inset shows the region where a spectrum image was acquired, along with the relative composition maps corresponding to the O *K* (left) and Fe $L_{2,3}$ (right) edges, in false color. The scale bar represents 5 nm. (b) O relative composition profile (in atomic percent) along the direction of the yellow arrow in panel a. The O atomic ratio of 57% at the center of the nanoparticles is consistent with a Fe_3O_4 magnetite structure (dashed line). The observed increase in the oxygen atomic ratio at the surface is well above the expected O atomic ratio of 60% for a γ-Fe_2O_3 structure, and it is attributed to the oleic acid attached to the surface.

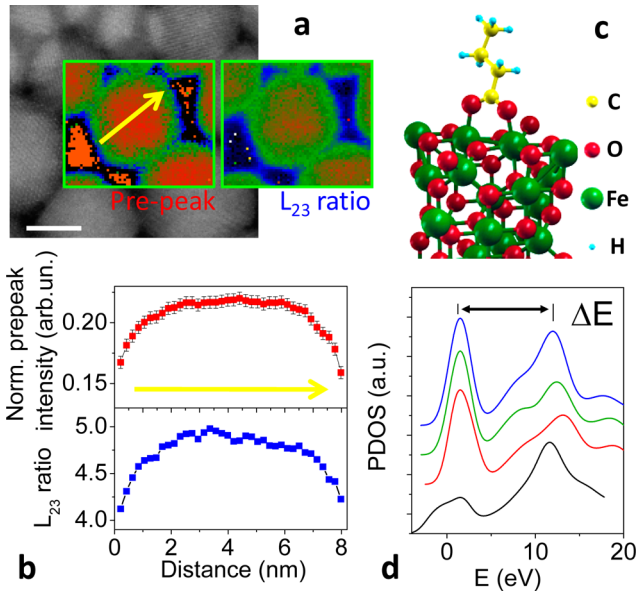

Figure 3. Experimental and theoretically spatially resolved EELS fine structure. (a) Z-contrast images of Fe_3O_4 nanoparticles. The inset shows the region where a spectrum image was acquired, along with the prepeak and the $L_{2,3}$ intensity ratio maps, in false color. The scale bar is 5 nm. (b) Normalized prepeak intensity and $L_{2,3}$ ratio profiles along the direction of the yellow arrow in panel a. (c) Minimal energy configuration of the iron oxide organic acid bond. (Only one surface unit cell is shown.) The oxygen of the carboxylic group completes the octahedral environment of the bonding iron ions, making their first coordination shell similar to bulk Fe_3O_4. (d) Simulated O *K* edge spectra for the configuration in panel c within the Z approximation. O prepeaks are aligned in energy for clarity. The prepeak intensity of the carboxylic oxygen (black) is smaller than that of the oxygen at the surface (red) and deeper within the bulk (green and blue as we move away from the surface); the prepeak reduction in panels a and b is then a signature of the organic acid−nanoparticle bond. Spectra have been displaced vertically for clarity.

We turn to theory to better interpret the variations of the EELS fine structure. Density functional theory (DFT)[24] reproduces the measured O *K*-edge fine structure of magnetite quite accurately (Supporting Information). To keep the computational cost affordable, we performed calculations of a deprotonated short-chain organic acid, butyric acid, adsorbed over the octahedral iron−oxygen terminated 100 surface of magnetite. Figure 3c illustrates the most stable configuration found after several simulated structural relaxations, starting from different initial configurations. We find a double-bonded configuration where the two oxygen atoms of the carboxylic group bond to two different Fe ions at the surface.

The calculated *K*-edge spectra from different oxygen ions in the DFT-predicted configuration are shown in Figure 3d. (All prepeaks are aligned at 1.5 eV, and the spectra vertically shifted for clarity.) The intensity of the prepeak feature coming from the oxygen atoms in the carboxylic group (black line) is indeed notably smaller, relative to the main peak, as compared with the surface (red line) and deeper bulk (green and blue lines) oxygen. Also, there is a shift of spectral weight so that the distance in energy between the prepeak and the main peak of the spectra from the carboxylic-group's oxygen is slightly reduced, as observed in the experiment. We deduce that the measured prepeak and ΔE reductions near the surface do not arise from the different environment of the oxygen atoms within the nanoparticle, but they are a fingerprint of the surface capping oleic acid.

According to the calculations, the adsorption energy is 2.4 eV, implying a strong covalent bond between the organic acid and the nanoparticle surface. Such a bond also contributes to chemical passivation of the surface, preventing further oxidation and the concomitant reduction of the magnetization. It might also favor, together with the high-temperature synthesis, the high crystal quality of the nanoparticle (Figure 1b,c) that is essential to obtain the high magnetization nanoparticles,[11] but the organic acid, however, affects the magnetic state of the nanoparticle in a more direct and unexpected way: by making the crystal environment and the occupancies of d orbitals in certain surface iron sites close to bulk Fe_3O_4. In bulk Fe_3O_4, the magnetization arises mainly from the majority electrons occupying d orbitals in octahedrally coordinated iron. Some of these d orbitals hybridize strongly with the oxygen p orbitals forming bonding and antibonding bands, which are all occupied in the bulk (Figure 4a). However, occupancies change at the bare surface,[25] as some of the spin majority states are pushed over the Fermi energy and become unoccupied (Figure 4b); the occupation of other d orbitals (not shown) also changes, and the magnetization density at the surface is greatly reduced.

The effect of the organic acid can now be understood. Figure 3c shows how, of the four Fe ions at the surface unit cell, two bond to the organic acid whereas the other two remain unbonded. Fe ions bonded to the organic acid oxygens have six O nearest neighbors at an average distance of 2.05 Å, close to the six neighbors at 2.10 Å in the bulk. As a result, their density of states and occupancies are similar to those of bulk Fe (Figure 4a,c, respectively). For the half of the surface Fe ions that do

dx.doi.org/10.1021/nl300665z | *Nano Lett.* 2012, 12, 2499−2503

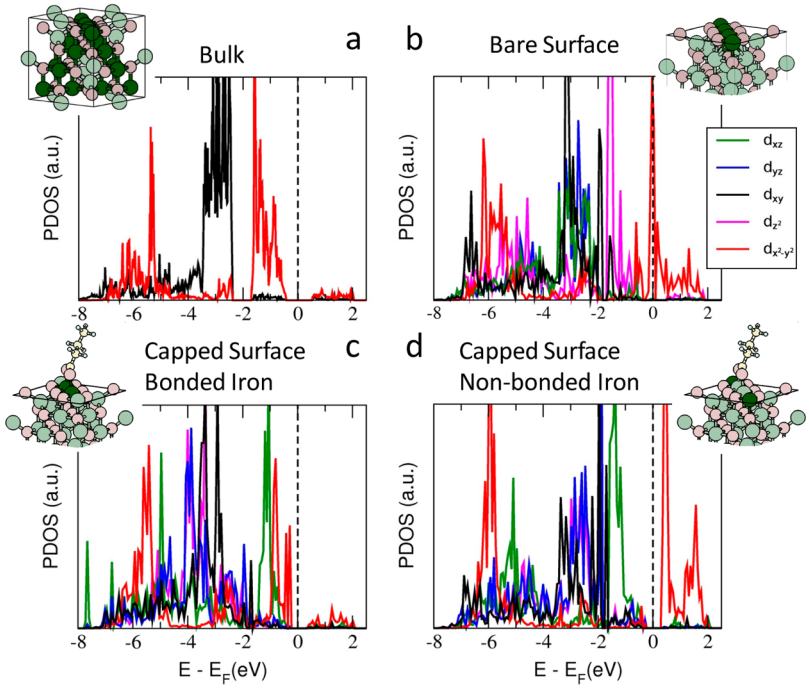

Figure 4. Density of states (DOS) projected over the majority spin d orbitals in the octahedral iron sites within different crystal environments. (a) Bulk Fe_3O_4 projected DOS. The degenerate e_g orbitals (red and magenta) point toward the neighboring oxygens and strongly hybridize with their p orbitals, giving rise to the bonding (around $E = -5$ eV) and antibonding (around $E = -1$ eV) density of states. The t_{2g} states (black, green, and blue, also degenerated by symmetry) hybridize less; almost all of their weight is in the band around 3 eV under E_F. The filling of the minority orbitals (not shown) is small, and the octahedral iron is highly polarized. (b) Bare (100) surface, projected DOS corresponding to octahedral iron at the surface. The structural surface reconstruction brings the in-plane oxygen ions closer to the iron ion, increasing the hybridization of the $d_{x^2-y^2}$ orbital (red). This orbital gets partially empty as it is pushed past the Fermi energy, resulting in a reduced magnetization. (c) Organic acid bonded to magnetite surface. DOS projected over octahedral iron bonded to the organic acid. Because of the influence of the oxygen ions in the carboxylic group, occupancies are very similar to the bulk case, and the reduction of magnetization at the surface is partially lifted. (d) Organic acid bonded to magnetite surface. DOS projected over the octahedral iron not bonded to the organic acid. Occupancies are very similar to the bare surface case (b).

not bond, the number of O nearest neighbors is five, as in the bare surface, and the average Fe−O distance is 1.92 Å, *only* 0.04 Å smaller than what we find at the bare surface.[25,26] This similarity is reflected again in the d orbital occupations, particularly in the unoccupied states, which resemble those of the bare surface (Figure 4d, similar to Figure 4b). The occupations of other orbitals (not shown) are also affected by the bonding, but the overall effect is that the capped surface magnetization density is 1 Bohr magneton per surface unit cell larger than the bare surface, representing an intermediate value between the more magnetic bulk and the less magnetic bare surface.

This unexpected enhancement of magnetism by an organic capping layer has strong implications for the optimization of a wide family of materials. Other magnetic nanoparticles used in medicine also possess the spinel structure and similar composition ($CoFe_2O_4$, $MnFe_2O_4$), and it is likely that the same phenomenon takes place in those systems. These results indicate that efforts to increase the number of organic molecules attached to the surface of nanoparticles will result in improved magnetic properties. Furthermore, functionalization processes that build onto the organic capping layer, crucial to control the physiological properties of the nanoparticles,[27] are expected to better preserve the magnetism than functionalization processes based on ligand exchange. In addition, the mechanism by which adsorbates restore the bulk crystal environment around surface ions and increase the surface magnetization naturally explains changes in surface magnetization of magnetite thin films.[16,17] Fields like spintronics[28,29] and others where surface magnetic dead layers are undesirable will also benefit from materials optimization guided by the understanding of this mechanism.

■ ASSOCIATED CONTENT

Ⓢ Supporting Information

Experimental details and DFT modeling details. This material is available free of charge via the Internet at http://pubs.acs.org.

■ AUTHOR INFORMATION

Corresponding Author

*E-mail: jsalafra@pas.ucm.es.

Present Address

▽Instituto de Ciencia de Materiales de Barcelona, Spain.

Author Contributions

#These authors contributed equally to this work.

Notes

The authors declare no competing financial interest.

■ ACKNOWLEDGMENTS

We thank Masashi Watanabe for the Digital Micrograph PCA plug-in. Some samples were kindly supplied by the Colloids and Surface Science group at Instituto de Ciencia de Materiales de Madrid. Research at ORNL (S.J.P. and M.V.) was sponsored by the Materials Sciences and Engineering Division of the U.S. Department of Energy (DOE). Research at UCM (J.G., J.S.) was supported by the ERC starting Investigator Award, grant no. 239739 STEMOX (J.S., J.G.) and by the Spanish MEC

2007-0086 (J.G.). Research at Vanderbilt was partially supported by the U.S. DOE grant DE-FG02-09ER46554 and the McMinn Endowment. Research at the UB was supported by the Spanish MICINN (MAT2009-08667 and CSD2006-00012) and Catalan DIUE (2009SGR856). Computations were supported by the National Center for Supercomputing Applications (U.S. Department of Energy, contract no. DE-AC02-05CH11231).

REFERENCES

(1) Batlle, X.; Labarta, A. *J. Phys. D: Appl. Phys.* **2002**, *35*, R15.
(2) Sun, S.; Zeng, H.; Robinson, D. B.; Raoux, S.; Rice, P. M.; Wang, S. X.; Li., G. *J. Am. Chem. Soc.* **2004**, *126*, 273−279.
(3) Park, J.; An, K.; Hwang, Y.; Park, J. G.; Noh, H. J.; Kim, J. Y.; Park, J. H.; Hwang, N. M.; Hyeon, T. *Nat. Mater.* **2004**, *3*, 891−895.
(4) Roca, A. G.; Morales, M. P.; O'Grady, K.; Serna, C. J. *Nanotechnology* **2006**, *17*, 2783−2788.
(5) Laurent, S.; Forge, D.; Port, M.; Roch, A.; Robic, C.; Vander Elst, L.; Muller, R. N. *Chem. Rev.* **2008**, *108*, 2064−2110.
(6) Scarberry, K. E.; Dickerson, E. B.; McDonald, J. F.; Zhang, Z. J. *J. Am. Chem. Soc.* **2008**, *130*, 10258−10262.
(7) Alexiou, C.; Schmid, R. J.; Jurgons, R.; Kremer, M.; Wanner, G.; Bergemann, C.; Huenges, E.; Nawroth, T.; Arnold, W.; Parak, F. G. *Eur. Biophys. J.* **2006**, *35*, 446−450.
(8) Lee, J. H.; Jang, J.; Choi, J.; Moon, S. H.; Noh, S.; Kim, J.; Kim, J. G.; Kim, I. S.; Park, K.,I.; Cheon, J. *Nat. Nanotechnol.* **2011**, *6*, 418−422.
(9) Roca, A. G.; Costo, R.; Rebolledo, A. F.; Veintemillas-Verdaguer, S.; Tartaj, P.; Gonzalez-Carreno, T.; Morales, M. P.; Serna., C. J. *J. Phys. D: Appl. Phys.* **2009**, *42*, 224002.
(10) Guardia, P.; Batlle-Brugal, B.; Roca, A. G.; Iglesias, O.; Morales, M. P.; Serna, C. J. *J. Magn. Magn. Mater.* **2007**, *316* (2), e756−e759.
(11) Pérez, N.; Bartolomé, F.; García, L. M.; Bartolomé, J.; Morales, M. P.; Serna, C. J.; Labarta, A.; Batlle, X. *Appl. Phys. Lett.* **2009**, *94*, 093108.
(12) Jana, N. R.; Chen, Y.; Peng, X. *Chem. Mater.* **2004**, *16*, 3931−3935.
(13) Park, J.; Joo, J.; Kwon, S.; Jang, Y.; Hyeon, T. *Angew. Chem., Int. Edn.* **2007**, *46*, 4630−4660.
(14) Pérez, N.; López-Calahorra, F.; Labarta, A.; Batlle, X. *Phys. Chem. Chem. Phys.* **2011**, *13*, 19485−19489.
(15) Batlle, X.; Pérez, N.; Guardia, P.; Iglesias, O.; Labarta, A.; Bartolomé, F.; García, L. M.; Bartolomé, J.; Roca, A. G.; Morales, M. P.; Serna, C. J. *J. Appl. Phys.* **2011**, *109*, 07B524.
(16) Kurahashi, M.; Sun, X.; Yamauchi, Y. *Phys. Rev. B* **2010**, *81*, 193402.
(17) Parkinson, G. S.; Mulakaluri, N.; Losovyj, Y.; Jacobson, P.; Pentcheva, R.; Diebold, U. *Phys. Rev. B* **2010**, *82*, 125413.
(18) White, M. A.; Johnson, J. A.; Koberstein, J. T.; Turro, N. J. *J. Am. Chem. Soc.* **2006**, *128*, 11356−11357.
(19) Roca, A. G.; Veintemillas-Verdaguer, S.; Port, M.; Robic, C.; Serna, C. J.; Morales, M. P. *J. Phys. Chem. B* **2009**, *113*, 7033−7039.
(20) Schattschneider, P.; Rubino, S.; Hébert, C.; Rusz, J.; Kuneš, J.; Novák, P.; Carlino, E.; Fabrizioli, M.; Panaccione, G.; Rossi, G. *Nature* **2006**, *441*, 486−488.
(21) Schattschneider, P.; Stöger-Pollach, M.; Rubino, S.; Sperl, M.; Hurm, C.; Zweck, J.; Rusz, J. *Phys. Rev. B* **2008**, *78*, 104413.
(22) Schattschneider, P.; Ennen, I.; Löffler, S.; Stöger-Pollach, M.; Verbeeck, J. *J. Appl. Phys.* **2010**, *107*, 09D311.
(23) Colliex, C.; Manoubi, T.; Ortiz, C. *Phys. Rev. B* **1991**, *44*, 11402−11411.
(24) Kohn, W.; Sham, L. J. *Phys. Rev.* **1965**, *140*, A1133−A1138.
(25) Pentcheva, R.; Wendler, F.; Meyerheim, H. L.; Moritz, W.; Jedrecy, N.; Scheffler, M. *Phys. Rev. Lett.* **2005**, *94*, 126101.
(26) Gaines, J. M.; Bloemen, P. J. H.; Kohlhepp, J. T.; Bulle-Lieuwma, C. W. T.; Wolf, R. M.; Reinders, A.; Jungblut, R. M.; Van Der Heijden, P. A. A.; Van Eemeren, J.; de Stegge, J.; Jonge, W. J. M. *Surf. Sci.* **1997**, *373*, 85−94.
(27) Gupta, A. K.; Gupta, M. *Biomaterials* **2005**, *26*, 3995−4021.
(28) Wolf, S. A.; Awschalom, D. D.; Buhrman, R. A.; Daughton, J. M.; von Molnar, S.; Roukes, M. L.; Chtchelkanova, A. Y.; Treger, D. M. *Science* **2001**, *294*, 1488−1495.
(29) Yoo, J.; Chen, C.; Jang, H. W.; Bark, C. W.; Prigodin, V. N.; Eom, C. B.; Epstein, A. J. *Nat. Mat.* **2010**, *9*, 638−642.
(30) Bosman, M.; Watanabe, M.; Alexander, D. T. L.; Keast, V. J. *Ultramicroscopy* **2006**, *106*, 1024−1032.